SOLUS | SMART OPTICAL AND ULTRASOUND DIAGNOSTICS OF BREAST CANCER

Project title: Smart Optical and Ultrasound Diagnostics of Breast Cancer

Grant Agreement: 731877

Call identifier: H2020-ICT-2016-1

Topic: ICT-29-2016 Photonics KET 2016

Deliverable 4.8: Final characterization of the SOLUS prototype

Leader partner: Beneficiary 1, POLIMI

Author(s): Alberto Dalla Mora (POLIMI), Giulia Maffeis (POLIMI), Laura Di Sieno (POLIMI), Giuseppe Di Sciacca (UCL), Simon Arridge (UCL), Andrea Farina (POLIMI), Mathieu Perriollat (CEA), Jean-Marc Dinten (CEA), Antonio Pifferi (POLIMI), Paola Taroni (POLIMI)

Work Package: 4

Estimated delivery: Month 60

Actual delivery: 30 October 2021

Type: Report

Dissemination level: Public

Table of contents

Abbreviations

C	Contrast
CNR	Contrast-to-Noise Ratio
DOT	Diffuse Optical Tomography
FOM	Figure of merit
IRF	Instrument Response Function
NL	Non-Linearity
US	Ultrasound
SL	Slope

1. Introduction

The aim of this document is the validation of the SOLUS prototype in laboratory settings to independently complement the clinical tests, but in this case under well-controlled conditions (e.g., known optical/geometrical properties of the perturbation, homogeneous surrounding structure). This deliverable concludes the activities of Work Package 4 and therefore builds up on several previous project results, some of which are listed here below being strictly connected with the content of this document:

- Deliverable D2.1, "Definition of paradigms representing exemplary breast lesions cases", public report. The document provides a set of simplified scenarios representing the clinical problem under study. In particular, two geometrical paradigms were identified, respectively referred to small (i.e., ~1 cm^3) and large (i.e., >1 cm^3) perturbations. These geometries have been implemented on phantoms for the validation of the SOLUS prototype.
- Deliverable D4.2, "Definition of protocols for system characterization", public report. This deliverable defines a novel protocol for performance assessment of both diffuse optical tomography (DOT) and multimodal DOT-ultrasound (US) systems since existing protocols are not specified for tomography. This protocol is based on three specific assays and considers figures of merit (FOMs) that are strictly linked to the DOT problem.
- Deliverable D4.4, "Provision of multi-modal phantom kit", confidential demonstrator. This deliverable provided to the SOLUS consortium suitable tools for the implementation of the protocol proposed in D4.2. In particular, a novel recipe to fabricate heterogeneous phantoms capable of providing both optical and ultrasound contrast was devised and utilized for the fabrication of a complete phantom kit. The delivered kit features different phantom bulks and perturbations that are specifically devised for the implementation of the optical and geometrical paradigms of D2.1 and of the assays proposed in D4.2. Considering the confidential nature of the accompanying document (D4.4), some necessary details about the phantom kit are given in the following sections.
- Deliverable D4.7, "Performance assessment of DOT with US priors", public report. The document validates the performances of the DOT reconstruction techniques guided by US priors developed within SOLUS. Further, it reports an improved definition of two figures of merit (contrast -C- and contrast-to-noise ratio -CNR-) related to one of the three assays of the protocol (i.e., the sensitivity test) proposed in D4.2, which permits a better link between the FOMs and the quality of the tomographic reconstructions.
- Deliverable D3.5, "Benchmark configuration and data assessing functional working of acquisition and processing hardware and software on the mockup system", public report. This document describes the final SOLUS prototype configuration, software and measurement sequences devised for the clinical use, which have been adopted also here for phantom measurements.

It is worth highlighting that all procedures, protocols, FOMs and implementation tools have been defined well before the system validation, granting an objective and standardized evaluation of the SOLUS system performances, following a virtuous approach fostered by an international growing community of researchers in the diffuse optics field, also supported by the European Commission through the organization of 2 workshops related to the "Performance Assessment and Standardisation in Biophotonics" during the last years (which have seen different SOLUS consortium partners deeply involved).

The present document is organized as follows. Section 2 deals with materials and methods that have been used for the validation. Section 3, 4 and 5 present, respectively, the results of the sensitivity, localization and quantification tests. Section 6 draws the main conclusions about the SOLUS system performances. Section 7 lists the relevant references to the literature.

2. Materials and Methods

Probe configuration

The SOLUS probe employed for this deliverable is probe #1, while a second equivalent probe (probe #2) is currently under fabrication. The presence of one optode not completely working (i.e., lasers not firing) inside probe #1 was already reported in D3.5: this failure was detected at CEA during initial tests. The full characterization of the probe, carried out at CEA required the direct access to some internal signals that

were accessible only before the complete probe sealing, as they were not expected to be useful during the normal use of the system (e.g., laser synchronization trigger). The data reported in D3.5 were therefore taken in this configuration, right before the final probe sealing. The probe was later sealed by VERMON and underwent different functional and safety tests at VERMON and SSI, which were all successful. The sealed probe, together with the other parts of the SOLUS system, was then sent to POLIMI for the validation in laboratory settings reported here. However, at POLIMI other 4 optodes resulted not fully operative (detector not responding and/or lasers not firing) right after unpacking the system. The probe was therefore reopened and inspected by both VERMON and MPD, in particular to exclude the presence of any water leakages from the internal water-cooling circuit that could have led to internal short circuits. The inspection allowed us to clearly exclude that possibility. The reason behind the failure is still under investigation and few hypotheses are under evaluation. As the inspection revealed localized dust-like stains, most probably the failure is due to mists released by the sealing glues during the curing stages. A particular attention is therefore being paid to this aspect during the fabrication of probe #2. Despite the presence of only 3 fully-working optodes (plus 4 more firing optodes, i.e., optodes with operating lasers, but not responding detector), initial results on phantoms were consistent to those reported in the previous deliverable D4.7, where 7 optodes were fully operative. Therefore, the probe can still be suitable for the proposed purpose and its performance has been evaluated here in its current state.

Protocol and phantoms

All the details about the SOLUS protocol can be found in public deliverables D4.2 and D4.7. Here we just briefly recall for convenience the meaning of the different tests there defined and the definition of the related FOMs, but we refer the reader to these previous documents for full details.

The SOLUS protocol has been defined to assess the performances of a generic DOT system or of a combined US-DOT system. It can also be applied to other multimodal systems as the morphological information in the tissue under investigation could in principle be provided by techniques other than US, like computed tomography or magnetic resonance imaging. It is based on three main tests to be performed: 1) sensitivity, 2) localization, and 3) quantification tests.

The **sensitivity** test permits to evaluate the system performance in detecting a perturbation inside a diffusive medium. This evaluation is based on two relevant figures of merit, i.e., ***contrast*** and ***contrast-to-noise ratio***. As specified in D4.7, with respect to the initial definition of D4.2, the two FOMs have been changed to grant a more direct link to the tomographic image quality, i.e.:

$$C_{a,s} = \frac{\tilde{\mu}_{a,s}^{Pert} - \tilde{\mu}_{a,s}^{Bulk}}{\tilde{\mu}_{a,s}^{Bulk}}; \qquad CNR_{a,s} = \frac{\tilde{\mu}_{a,s}^{Pert} - \tilde{\mu}_{a,s}^{Bulk}}{\sigma(\tilde{\mu}_{a,s}^{Bulk})},$$

where $\tilde{\mu}_{a,s}^{Pert}$ and $\tilde{\mu}_{a,s}^{Bulk}$ are the reconstructed absorption (***a***) or reduced scattering (***s***) coefficients inside (*Pert*) or outside (*Bulk*) the perturbation volume, while $\sigma(\tilde{\mu}_{a,s}^{Bulk})$ is the standard deviation of the reconstructed optical properties in the bulk volume. It is worth noting that the expected value of C is known on phantoms, where conventionally true optical properties have been assigned thanks to the accurate characterization of the perturbation and bulk materials using state-of-the-art spectroscopy systems. Equivalently, for the same reason the expected sign of CNR is known (negative or positive depending on conventionally true optical properties). Therefore, the ideal value of the measured C is the expected value, while the ideal value of the CNR is infinite (i.e., absence of fluctuation in the optical properties of the background)

The **localization** test is meant to measure the system performance in retrieving both the correct position and size of the perturbation. Again, the test is based on the quantification of two FOMs, i.e., ***displacement*** error (ε) and ***broadening*** (σ), defined as:

$$\varepsilon_{x_i} = \tilde{x_i} - x_i; \qquad \sigma_{x_i} = RMS(\tilde{x_i}) - \Delta x_i$$

where $\tilde{x_i}$ and x_i are, respectively, the retrieved and nominal positions of the perturbation along a direction x_i, while $RMS(\tilde{x_i})$ is the root mean square width of the reconstructed perturbation and Δx_i is the nominal size of the inclusion, both in the same direction x_i. For both FOMs, the ideal value is zero (i.e., perfect localization and absence of broadening).

The **quantification** test aims to assess the absolute and relative quantification capability of the optical properties of a localized perturbation. This test is divided into two sub-tests (accuracy and linearity). The ***accuracy*** one assesses the system capability in retrieving the true optical properties of the perturbation. This performance is measured through the errors in retrieving the absorption (ε_a) and the reduced scattering (ε_s) coefficients, defined as:

$$\varepsilon_a = \frac{\tilde{\mu}_a^{Pert} - \mu_a^{Pert}}{\mu_a^{Pert}}; \qquad \varepsilon_s = \frac{\tilde{\mu}_s'^{Pert} - \mu_s'^{Pert}}{\mu_s'^{Pert}}$$

where $\tilde{\mu}_a^{Pert}$ and $\tilde{\mu}_s'^{Pert}$ are the retrieved optical properties inside the perturbation and, equivalently, μ_a^{Pert} and $\mu_s'^{Pert}$ are the conventionally true values. For both FOMs, the ideal value is zero (i.e., perfect optical property retrieval). The ***linearity*** sub-test instead is meant to assess the system capability to linearly follow changes in the optical properties of the perturbation without distortions. In this case a linearity plot (e.g., $\tilde{\mu}_a^{Pert}$ vs. μ_a^{Pert}) is fitted using a second order polynomial ($y = ax^2 + bx + c$; where $y = \frac{\tilde{\mu}_a^{Pert}}{\gamma}$, $x = \frac{\mu_a^{Pert}}{\gamma}$, and γ = 0.1 cm^{-1} -for absorption linearity- or 1 cm^{-1} -for scattering linearity-) and evaluating the slope (SL) and non-linear (NL) terms as:

$$SL = 2ax + b; \qquad NL = \frac{2a}{b}\Delta x$$

in which x is a function of the targeted optical property at which the SL is evaluated, and, equivalently, Δx is a function of the change in the targeted optical property over which the NL is evaluated. The ideal value of the SL FOM is 1 (i.e., the measured optical property change matches the true optical property change) when evaluating $\tilde{\mu}_a^{Pert}$ vs. μ_a^{Pert} and $\tilde{\mu}_s'^{Pert}$ vs. $\mu_s'^{Pert}$. The ideal value of NL is instead 0 (i.e., data are best fitted with a straight line, a = 0).

The phantoms used to assess the performances of the SOLUS prototype are those described in deliverable D4.4 (“Provision of multi-modal phantom kit”) and in Refs. [1]-[2]. In few words, the phantoms are made of two different kinds of silicone: a silicone rubber (Ecoflex 00-30, Smooth-On, Inc. PA, USA; in the following “Ecoflex”) and a silicone elastomer (Sylgard S184, Dow Corning Corp. CA, USA; in the following “Sylgard”). The use of two different materials allows one to have an echogenic contrast, independent of the optical one, since the Ecoflex shows higher echogenicity than Sylgard. More in detail, for each set (characterized by given optical properties, see below for details) a bulk was realized (whose dimensions are 12 x 100 x 4 cm^3) hosting 2 cylindrical cavities: a “small” one (diameter of 1.1 cm, height: 1 cm; overall volume about 1 cm^3) and a “big” one (diameter of 2.2 cm, height: 1.5 cm; overall volume about 6 cm^3). Moreover, 3 slices with the same surface (12 x 10 cm^2), featuring different thicknesses (0.5, 1.5 and 2.5 cm), have been produced.

The inclusions (i.e., the cylinders which perfectly fit the cylindrical cavities in the bulk) can be made of Ecoflex (i.e., no US contrast) or Sylgard. In this deliverable, when speaking of inclusions, we refer to the Sylgard inclusions while the Ecoflex ones were used only to fill the cavities in the homogeneous case. For what concerns the optical properties, the bulk was fixed at a nominal absorption coefficient of 0.08 cm^{-1} and a reduced scattering coefficient of 12 cm^{-1}. On the other hand, Sylgard inclusions span a wide range of absorption values (from 0.04 to 0.48 cm^{-1} in steps of 0.04 cm^{-1}) and reduced scattering coefficients (from 6 to 18 in steps of 6 cm^{-1}). It has to be noted that with respect to the phantom kit reported in D4.4, some modifications to the nominal optical properties have been done. Indeed, we noticed that the experimental characterization was not perfectly matched with the nominal optical properties. To better match the conventionally true values, we changed the nominal values (keeping the reference wavelength at 690 nm). The few phantoms which were far from the new nominal values were refabricated. Table 1 reports both the current and the previous (i.e., those reported in D4.4) nominal optical properties of the bulk and inclusions here used, at the wavelength of 690 nm.

Table 1. Nominal optical properties of the bulk and inclusions used for the SOLUS prototype characterization. Both current and previous nominal values (i.e., those reported in D4.4) are displayed.

Type	Material	μ_s' (cm^{-1})		μ_a (cm^{-1})	
		Current	Previous	Current	Previous
Bulk	Ecoflex	12	10	0.08	0.1
Inclusions	Sylgard	6	5	0.08	0.1
Inclusions	Sylgard	12	10	0.04	0.05
Inclusions	Sylgard	12	10	0.08	0.1
Inclusions	Sylgard	12	10	0.16	0.2
Inclusions	Sylgard	12	10	0.32	0.4
Inclusions	Sylgard	12	10	0.48	0.6
Inclusions	Sylgard	18	15	0.08	0.1

To take into account the spectral behaviour of the phantoms (both Sylgard and Ecofelx ones) a spectral characterization has been done using a state-of-the-art diffuse optics spectroscopy system [3]. In Table 2 and Table 3 their absorption and reduced scattering coefficients, respectively, are reported at the wavelengths of the SOLUS prototype. These are in the following assumed as the conventionally true values for the calculation of the different related FOMs (e.g., accuracy, linearity, etc.). With respect to the previously published deliverable (e.g., D4.6 "Performance assessment of the single optode" and D4.7 "Performance assessment of DOT with US priors"), we modified the nominal wavelengths of the SOLUS prototype to better match the measured values. In the following, we will refer to the wavelengths with the new nomenclature.

Table 2. Conventionally true values (in cm^{-1}) of absorption coefficient at the SOLUS prototype wavelengths for all phantoms.

	μ'_s (cm^{-1})	**μ_a (cm^{-1})**	**Wavelength (nm)**							
			640	**675**	**830**	**905**	**930**	**970**	**1020**	**1050**
SYLGARD	**6**	**0.08**	0.087	0.084	0.086	0.137	0.099	0.088	0.140	0.096
	12	**0.04**	0.036	0.035	0.037	0.085	0.050	0.040	0.090	0.047
		0.08	0.084	0.081	0.082	0.131	0.094	0.084	0.133	0.090
		0.16	0.133	0.129	0.128	0.176	0.141	0.128	0.180	0.135
		0.32	0.263	0.252	0.251	0.301	0.260	0.245	0.292	0.258
		0.48	0.392	0.379	0.374	0.420	0.374	0.364	0.412	0.366
	18	**0.08**	0.084	0.082	0.081	0.127	0.094	0.082	0.132	0.088
ECO-FLEX	**12**	**0.08**	0.090	0.082	0.075	0.139	0.072	0.072	0.121	0.071

Table 3. Conventionally true values (in cm^{-1}) of reduced scattering coefficient at the SOLUS prototype wavelengths for all phantoms.

	μ'_s (cm^{-1})	**μ_a (cm^{-1})**	**Wavelength (nm)**							
			640	**675**	**830**	**905**	**930**	**970**	**1020**	**1050**
SYLGARD	**6**	**0.08**	7.07	6.54	4.84	4.26	4.10	3.85	3.58	3.43
	12	**0.04**	12.71	11.72	8.57	7.51	7.21	6.76	6.27	6.00
		0.08	12.94	11.95	8.76	7.70	7.39	6.93	6.43	6.16
		0.16	12.24	11.32	8.34	7.34	7.05	6.62	6.15	5.89
		0.32	13.81	12.74	9.31	8.16	7.83	7.35	6.81	6.52
		0.48	13.17	12.13	8.83	7.73	7.41	6.95	6.43	6.15
	18	**0.08**	20.21	18.59	13.46	11.76	11.27	10.55	9.75	9.32
ECO-FLEX	**12**	**0.08**	14.72	13.43	9.42	8.12	7.75	7.21	6.61	6.29

Measurement procedures

A set of measures was performed on the silicone phantoms described above in order to test tomographic capabilities of the SOLUS prototype for the different wavelengths and for different choices of the inclusion, as reported in Table 4. The bulk and the top layers always share the same optical properties.

These tests were pursued both for the small (1 cm^3) and the big (6 cm^3) inclusions, thus evaluating also the effect of the inclusion size. Accordingly, the top layer was chosen based on the paradigm illustrated in Deliverable 2.1: 0.5 cm for the small inclusion, 1.5 cm for the big one. Moreover, when the target was the small inclusion, the big inclusion slot was occupied with a neutral Ecoflex filler with the same optical properties of the bulk. That generated a reasonable extension of homogenous area on the phantom. The analogue was done when the target was the big inclusion.

All measures were performed after the probe issues detailed in the previous Section, with the probe configuration depicted in Figure 1. At this stage, in order to work in the safest conditions, measures involved only optical acquisitions, excluding ultrasounds images.

Each measure, *i.e.*, each entry of Table 4 focusing on a single inclusion (small or big), was articulated in 4 stages (Figure 2):

1. light trimming, just above the neutral filler, in vertical position;
2. homogeneous acquisition, in the same position of stage 1;
3. heterogeneous acquisition, centering the small/big inclusion, in vertical position;
4. heterogeneous acquisition, centering the small/big inclusion, in horizontal position.

Table 4. Combinations of optical and geometrical conditions used for the SOLUS prototype characterization. The background colours highlight alternate conditions.

Bulk		Perturbation		Top layer	
Nominal μ_a^{Bulk} (cm^{-1})	Nominal $\mu_s'^{Bulk}$ (cm^{-1})	Nominal μ_a^{Pert} (cm^{-1})	Nominal $\mu_s'^{Pert}$ (cm^{-1})	Thickness (cm) (1 cm^3 pert. volume)	Thickness (cm) (6 cm^3 pert. volume)
0.08	12	0.04	12	0.5	1.5
0.08	12	0.08	12	0.5	1.5
0.08	12	0.16	12	0.5	1.5
0.08	12	0.32	12	0.5	1.5
0.08	12	0.48	12	0.5	1.5
0.08	12	0.08	6	0.5	1.5
0.08	12	0.08	18	0.5	1.5

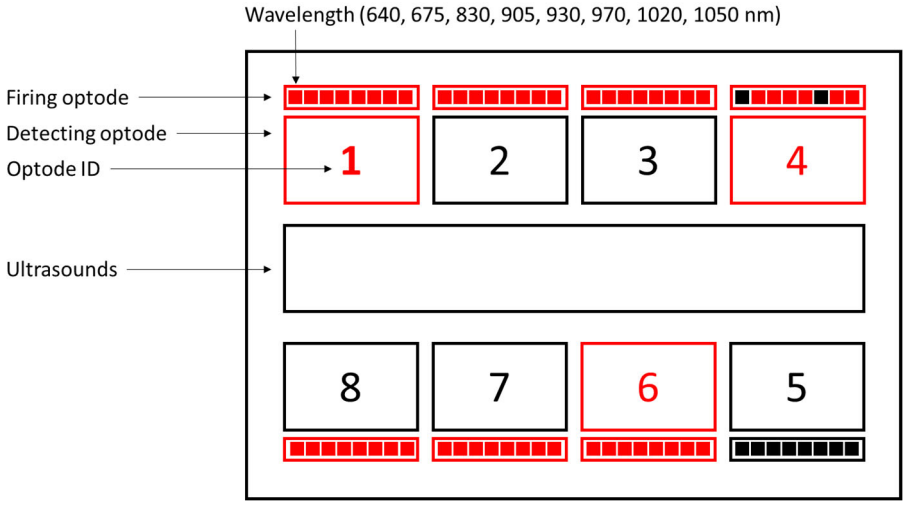

Figure 1: Current status of the SOLUS probe. Red colour highlights the active elements, limited to optical parts.

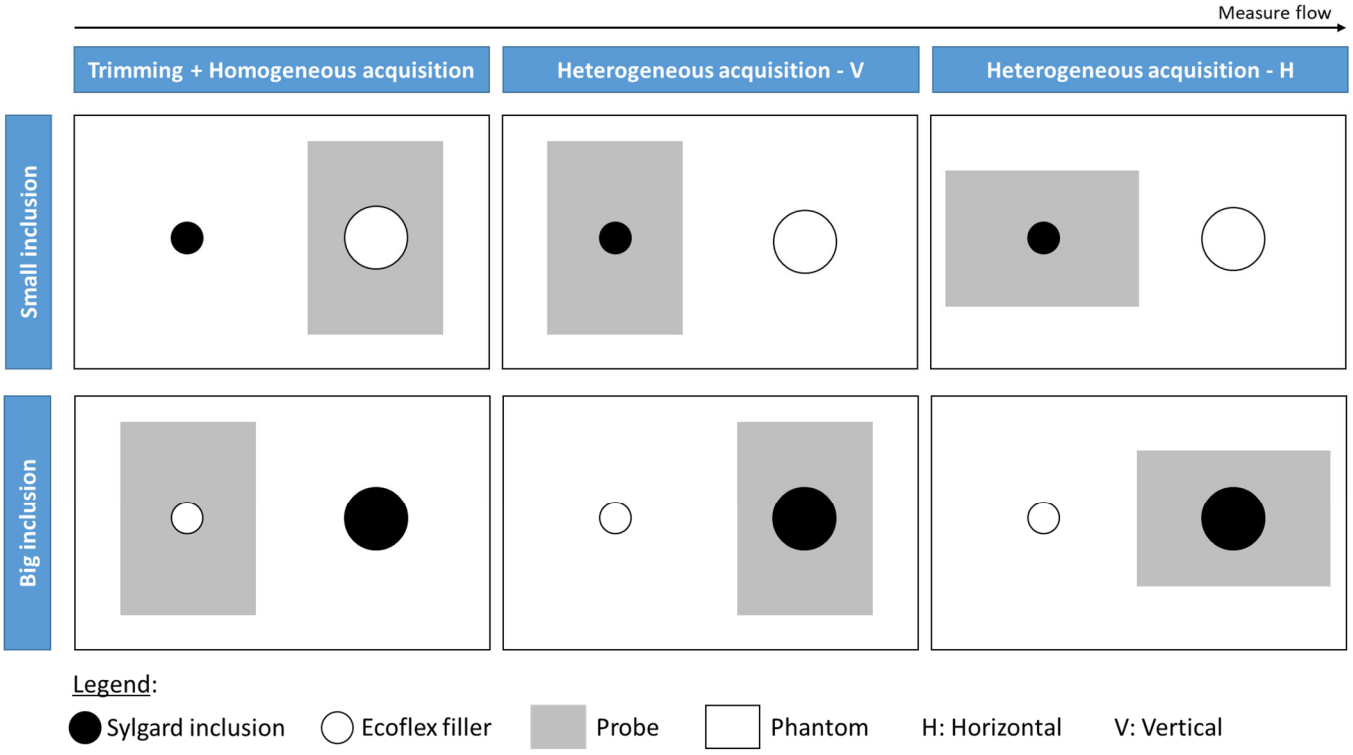

Figure 2: Scheme of the measure procedure.

The trimming procedure (stage 1) consists in the tuning of the collected light intensity to reach a specific count rate target, which means activating a certain number of pixels in each detector. Acquisitions at stages 2, 3 and 4 were performed with these amounts of enabled active areas.

The acquisition in horizontal position (stage 4) enriches information for the final tomographic reconstructions: the final retrieved perturbation optical properties result from the average outcome of the two measurements.

During an acquisition, sources sequentially emit light, firing optode by firing optode and wavelength by wavelength, while collection occurs simultaneously over the available detectors. The parameters chosen for these acquisitions were:

- Count rate target: 10^5 photons/s
- Acquisition time: 10 ms
- Gates: 13 gates (temporal width of 3 ns) progressively delayed at steps of 250 ps

In order to minimize distortions due to ambient light, the probe and the phantom were covered by a blackout fabric during the acquisitions.

Even though ultrasounds did not take part in measurements, the contact between the probe and the phantom was always mediated by an optically-tested ultrasound gel (Parker Laboratories Polysonic Ultrasound Lotion), so that to improve material mismatch and mimic clinical conditions on the optical side.

An Instrument Response Function (IRF) was acquired for each inclusion size. An IRF characterizes the time resolution of the instrument as a whole and it is crucial for the reconstruction of the absorption and scattering coefficients of the sample. Ideally, it should be acquired by placing the source and the detector face to face, but this is unfeasible in the case of the SOLUS probe. This is the reason why a SOLUS IRF box has been conceived and 3D printed (Figure 3), following the principle reported in Ref. [4]: the probe is inserted in the specially designed slot (top part of the IRF box), which has a mask on the bottom that perfectly reproduces the probe geometry. A standard measure is performed: light penetrates in the lower part of the box, which is empty, it propagates through some reflections and then goes back to the probe, where it is collected by the detector. This device allows one to acquire the IRF in a reproducible manner, taking into account the complex geometry of the probe.

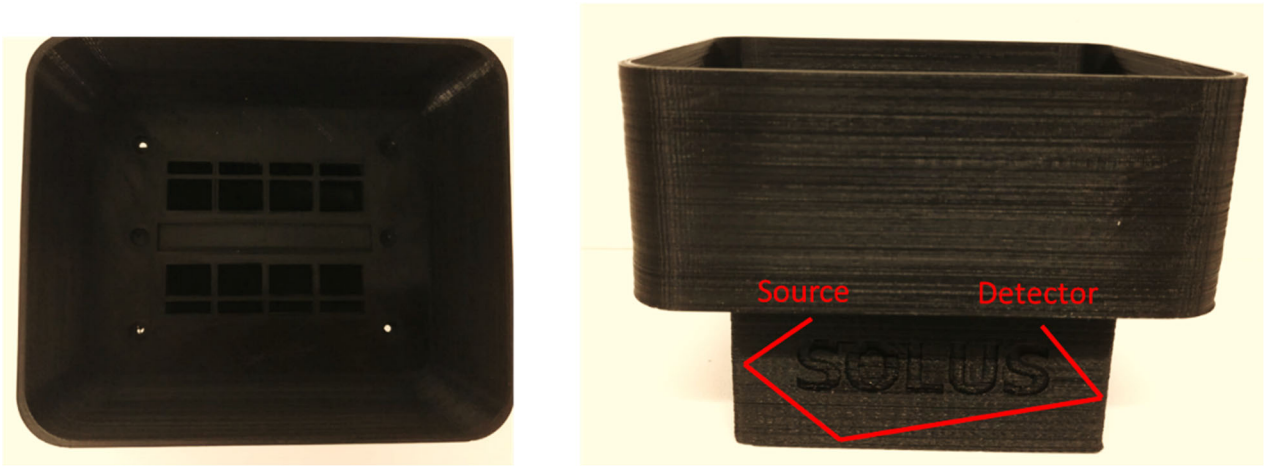

Figure 3: SOLUS IRF box, top view (left) and front view (right).

DOT reconstruction settings and figures of merit extraction

Priors were extracted as per D4.7. Instead of acquiring an US image for each phantom, a different approach has been chosen. Starting from two US images – one for the large inclusion and one for the small one – two 3D priors were extracted. The depth of each prior was set as a second step. No translation along x and y directions was necessary due to the chosen experimental conditions i.e. the centre of the inclusion along the xy plane was coincident with the centre of the probe on the same plane.

The sensitivity and accuracy figures of merit were extracted by evaluating the average tomographic reconstruction value in the region identified by the corresponding US prior. In so doing the displacement and broadening of the reconstructed inclusion with respect to the ground truth were dependent solely on the US prior extraction procedure. Following, we display the displacement as the Euclidean distance between the centre of the prior and the centre of the ground truth. The broadening is expressed as a single value by taking the average broadening of the reconstructed inclusion with respect to the ground truth. The broadening along each direction was taken to be the difference between the maximum elongation of the ground truth and of the prior along the axis. As the linearity FOMs depend, respectively, on x and Δx, the SL parameter has been reported as a function of x, while the NL has been computed by assuming Δx = 1 (dimensionless, for an absorption perturbation, see D4.2).

3. Sensitivity test

Example of Tomographic Reconstruction

Figure 4 shows an example of a tomography obtained using the SOLUS system on a silicone phantom bearing a 6 cm^3 absorption inhomogeneity buried at 1.5 cm depth. The top-left panel shows the US image where it is possible to identify the lesion due to the contrast in the ECOFLEX-SYLGARD heterogeneous structure. The top-right panel displays the corresponding extruded 3D shape generated from the segmentation of the US image. The bottom panel shows the reconstructed absorption coefficient using the *a priori* US information and a regularisation level of 0.1. Each small square corresponds to a different slice in depth of the reconstruction in steps of 2 mm. The inhomogeneity is localised at a proper depth, with a positive optical contrast (yellow colour) at all wavelengths as expected since the added absorber in the perturbation (black toner) is almost flat over the whole spectrum.

Contrast

Figure 5 shows the contrast in absorption for the two sizes of inclusions (volume in the legend – cm^3) for the 8 wavelengths. Moving from left to right panels, the nominal absorption coefficient of the inclusion (value reported - in cm^{-1} - in the title of the graphs) increases. The black line reports the expected contrast calculated on the basis of the optical characterisation of the materials. In general terms, the SOLUS system is capable to detect the inhomogeneity with a contrast that is increasing for higher values of the μ_a^{Pert} in the

homogeneity, as expected, reaching up to a factor of 3-4 (i.e., 300%-400% increase with respect to the background) which grants a good visibility of the lesion. Yet, the results are rather cluttered for different wavelengths. Indeed, this is the key limitation observed in the laboratory test of the instrument, that is a certain level of noise in the reconstruction. This limitation could be due to the important reduction in the number of collecting optodes (from 8 to 3) and could be lessened by the second release of the probe, which is now under finalization.

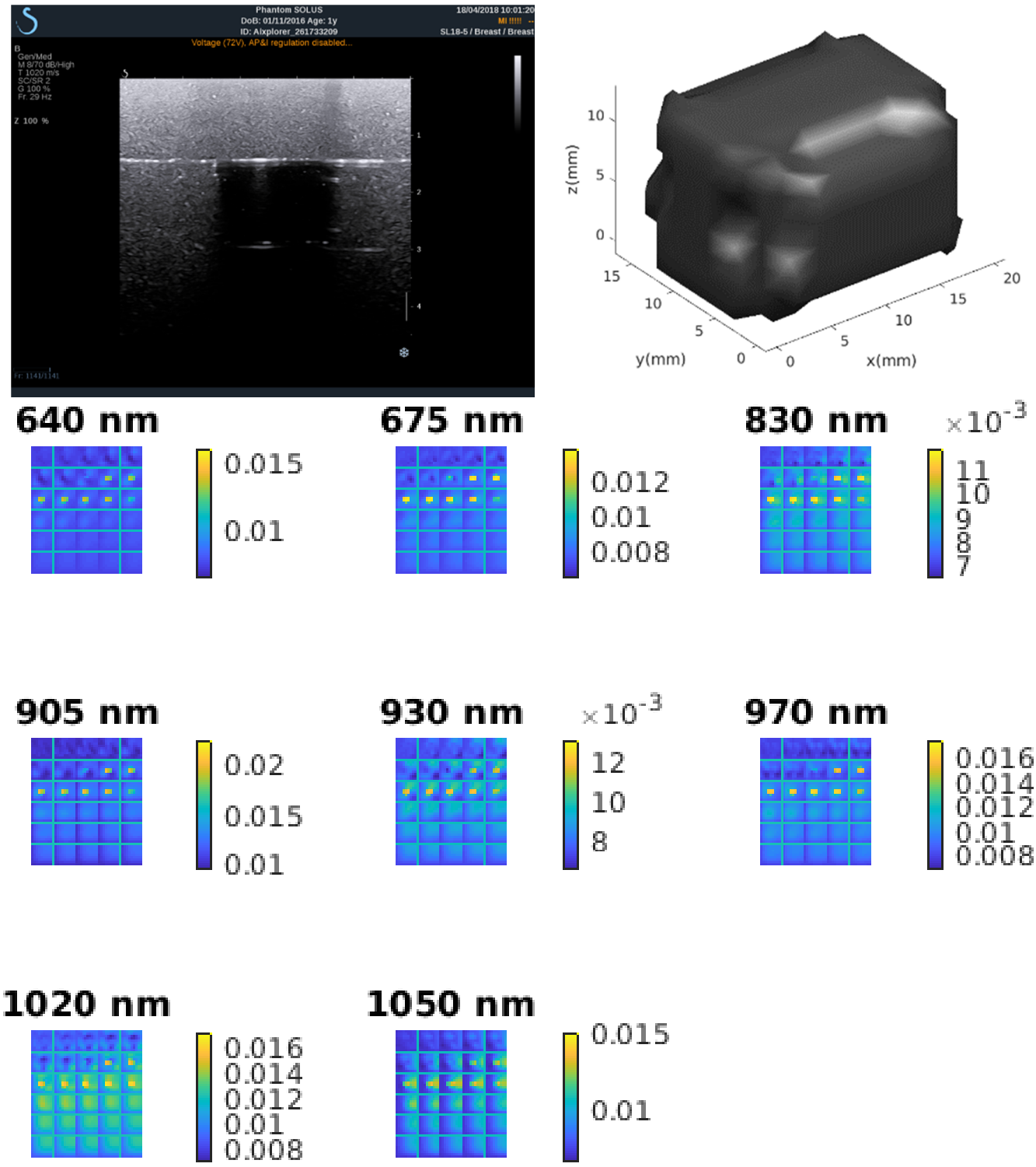

Figure 4. Example of B-mode US image, extracted prior and tomographic reconstruction of absorption for the phantom condition at the third line of Table 4 (large perturbation) and regularisation parameter of 0.1. For each wavelength a slice view of the 3D reconstruction is shown, top left slice is the top of the phantom and bottom right is its bottom.

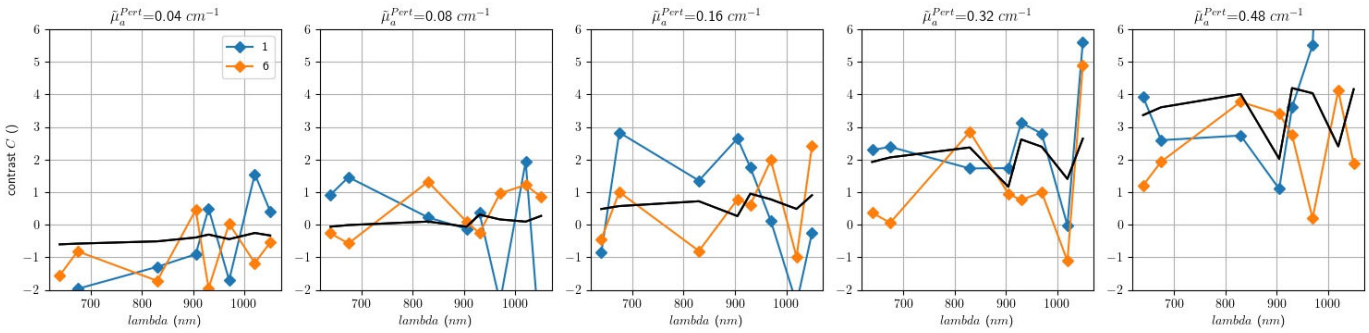

Figure 5. Absorption contrast (y-axes) as a function of wavelength (x-axes) for the two sizes of inhomogeneities (volume in the legend in cm³). From left to right, plots correspond to increasing values of the nominal absorption coefficient of the perturbation. The black line is the expected contrast. The regularization parameter is set to 0.01.

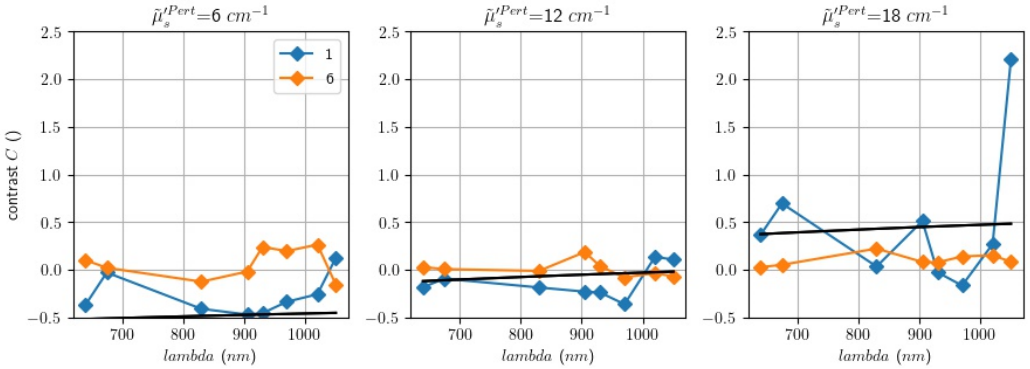

Figure 6. Scattering contrast (y-axes) as a function of wavelength (x-axes) for the two sizes of inhomogeneity (volume in the legend in cm³). From left to right, plots correspond to increasing values of the nominal scattering coefficient of the perturbation. The black line is the expected contrast. The regularization parameter is set to 0.1.

For the scattering perturbations (

Figure 6), two inhomogeneities were tested, that are a lower (6 cm^{-1}) and a higher (18 cm^{-1}) perturbation than the bulk (12 cm^{-1}), respectively. In general, as expected, for the smaller perturbation, for most of the wavelengths, correspondingly negative and positive contrast is observed. Conversely, the larger perturbation exhibits mostly a slightly positive contrast. Data are quite dispersed, with no regular trend with wavelength. In the case of scattering, we used a higher regularization parameter of 0.1 due to the smaller effects of scattering inhomogeneities on the DTOF. The adoption of different regularization parameters for absorption and scattering is not a big issue. Both parameters are always used as free parameters in reconstruction. Simply, output data are extracted from different reconstructions.

CNR

Figure 7 shows the CNR with the very same arrangement as in Figure 5. Moving from left to right across plots, the nominal absorption coefficient of the inclusion increases. The lesion is visible with a reasonable CNR for the two highest perturbations, while for lower optical contrast some wavelengths are not emerging over the background noise level. For the first set of lesions (left column) the CNR is mostly negative just because we retained the sign of the optical contrast which is negative (lesion absorption lower than background).

Similarly, Figure 8 shows the CNR with the same arrangement as in

Figure 6. Again, the general increasing trend of μ_s^{Pert} is visible but data are quite dispersed, with no regular trend with wavelength.

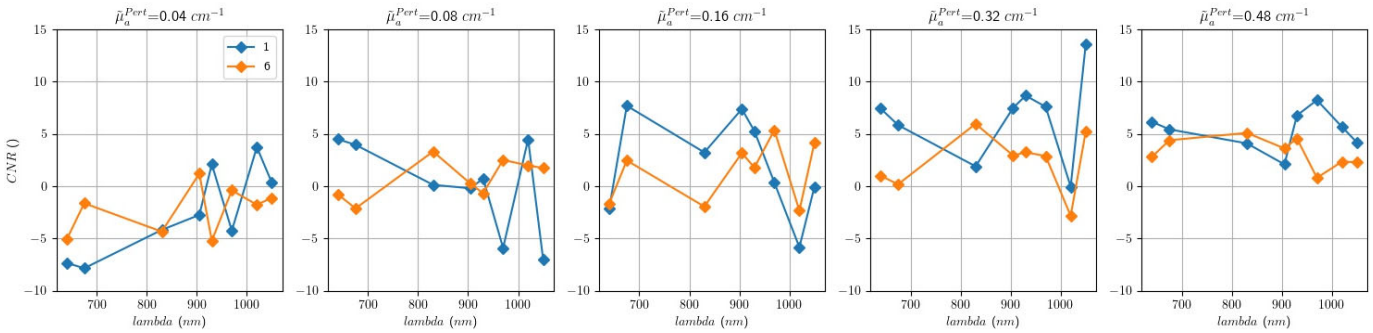

Figure 7. Absorption CNR (y-axes) as a function of wavelength (x-axes) for the two sizes of inhomogeneities (volume in the legend in cm³). From left to right, plots correspond to increasing values of the nominal absorption coefficient of the perturbation. The regularization parameter is set to 0.01.

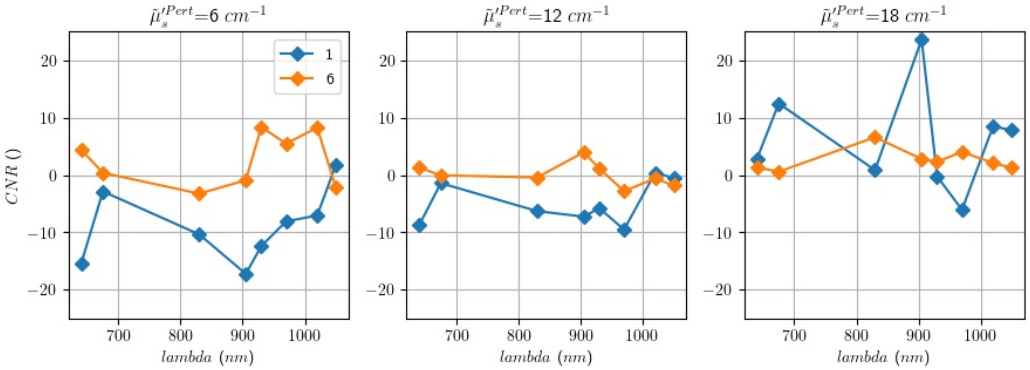

Figure 8. Scattering CNR (y-axes) as a function of wavelength (x-axes) for the two sizes of inhomogeneities (volume in the legend in cm³). From left to right, plots correspond to increasing values of the nominal scattering coefficient of the perturbation. The regularization parameter is set to 0.1.

4. Localization test

Displacement

The displacement error for the 1 cm³ and 6 cm³ absorption perturbation is <1 mm and <2 mm, respectively. Also the scattering perturbation is retrieved with the same small displacement error. This optimal localisation performance is a clear consequence of the reconstruction strategy making full use of the *a priori* US information. Therefore, in this framework this figure must be understood more in terms of self-consistence with the regularization approach, and it is clearly linked to the actual accuracy in the US localisation.

Broadening

The broadening is quite limited, both for the absorption and for the scattering inhomogeneities, with values <2 mm and <4 mm for the smaller and the larger lesion, respectively.

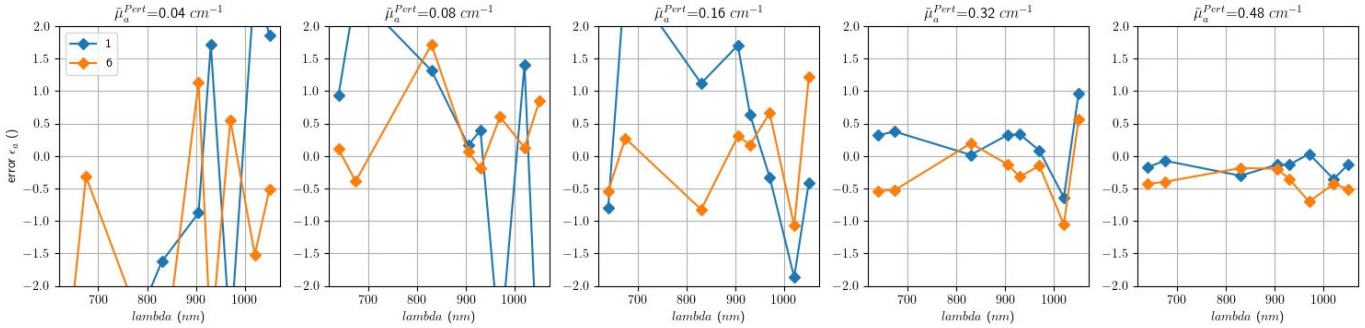

Figure 9. Absorption accuracy (error, y-axes) as a function of wavelength (x-axes) for the two sizes of inhomogeneities (volume in the legend in cm³). From left to right, plots correspond to increasing values of the nominal absorption coefficient of the perturbation. The regularization parameter is set to 0.01.

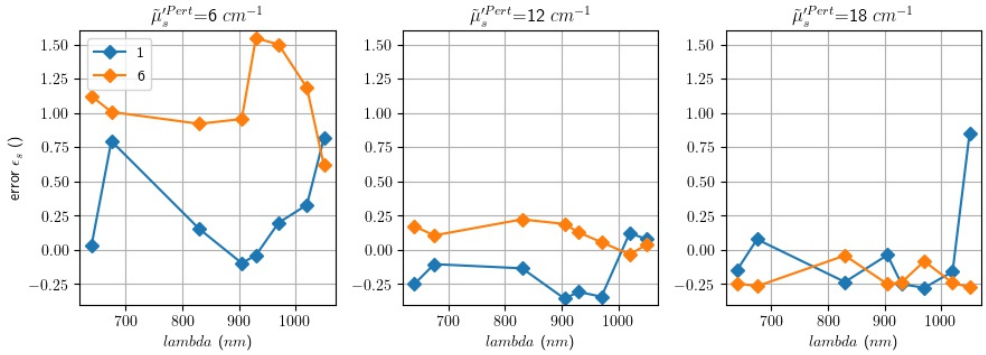

Figure 10. Scattering accuracy (error, y-axes) as a function of wavelength (x-axes) for the two sizes of inhomogeneity (volume in the legend in cm³). From left to right, plots correspond to increasing values of the nominal scattering coefficient of the perturbation. The regularization parameter is set to 0.1.

5. Quantification test

Accuracy

Figure 9 shows the accuracy on absorption reconstruction for the two sizes of inclusions (volume in the legend – cm³) for the 8 wavelengths. Moving from left to right panels, the nominal absorption coefficient of the inclusion increases (value - in cm^{-1} - reported in the title of the graphs). The plotted figure of merit is the relative error with respect to the expected value, that is ε_a. A perfect accuracy leads to ε_a = 0. As can be observed, for smaller perturbations the error is larger, and gets acceptable only for the two largest perturbations (i.e., $\mu_a^{Pert} \geq 0.4$ cm^{-1}). In this case, the error is mostly an underestimation of the perturbation. This is a well-known effect due to the regularization, which tends to reduce the absolute estimate of the perturbation properties. We tested also lower values for the regularization parameters, but this increases the noise in the reconstruction, which led to choose 0.01 as the best regularisation parameter as a good trade-off between noise and regularization artefacts.

Similar performances are observed for the two scattering perturbations (Figure 10), with an error in the order of 0.5-1.0 (i.e., 50-100%) for the lower scattering inhomogeneity, which reduces to an underestimation of around 0.25 (i.e., 25%) for the higher scattering inhomogeneity.

Linearity

Figure 11 shows a linearity plot of the reconstructed $\tilde{\mu}_a^{Pert}$ as a function of the true μ_a^{Pert}. For the different wavelengths (panels). In general, there is a certain linearity trend with reconstructed properties twisted around the expected value (black line). This indeed is the most important figure-of-merit for the SOLUS prototype, since the final goal is the discrimination of lesion types based on their relative compositions. Errors in accuracy are acceptable if linearity is preserved. Again, the problem here is the noise, causing a spreading of values around the linearity line.

From the plot of Figure 11 it is possible, as explained in Section 2, to extract the two FOMs for linearity, which are the slope *SL* and the non-linearity *NL*. First, data in Figure 11 are interpolated with a second order polynomial and then the two FOMs are extracted as described above. Figure 12 shows the plot of the *SL* as a function of the absorption perturbation for different wavelengths (panels). The expected value (black line) is 1. Generally speaking, the sign of *SL* is positive for all wavelengths apart from 1020 nm. In this case, the different absorption peaks of the two silicone components of the background and inclusion could play a confounding effect. Results are better for the larger inclusion with values closer to the expectation, while more significant deviations are observed in the case of the smaller perturbation. Yet, there seems to be no systematic effect, and the reason for deviation seems to be ascribed again to the noise in reconstruction which could be more severe for the smaller volume.

Figure 13 shows the non-linearity *NL* plot with the same arrangement of the previous figure. The plot is always constant with respect to the perturbation by definition, but we preferred to use the very same figure format for consistency with the previous FOM. The expected value for *NL* is 0 (black line) that is no deviation from a linearity trend. In practically all cases there is a negative *NL*, which means there is a progressive underestimation of the optical inhomogeneity for an increasing difference with respect to the background. This behaviour is expected and is probably caused by the Born approximation in the reconstruction model, which is needed to obtain a linear inverse problem which can be solved with computational time low enough to be compatible with the clinical workflow. In any case, the deviation from linearity is not large, mostly in the order of -20%, meaning that for an increase in the perturbation by 100% there is an underestimation of the recovered properties of 20%. We note here that *NL* must not be simply considered as the second derivative of the second-order polynomial fit. Rather, as commented above in the definition of *NL*, it carries information on the over- or under-estimation of the absorption perturbation.

For the scattering inhomogeneities, the linearity plot (Figure 14) is reasonable for the smaller perturbation, but is largely flat for the larger one. This is reflected in the *SL* values (Figure 15) that are closer to 1 for the small perturbation and almost null for the larger one. The *NL* plot (Figure 16) is always negative (apart from the 830 nm) which means a trend of saturation, possibly ascribed, as for the absorption, to the Born approximation.

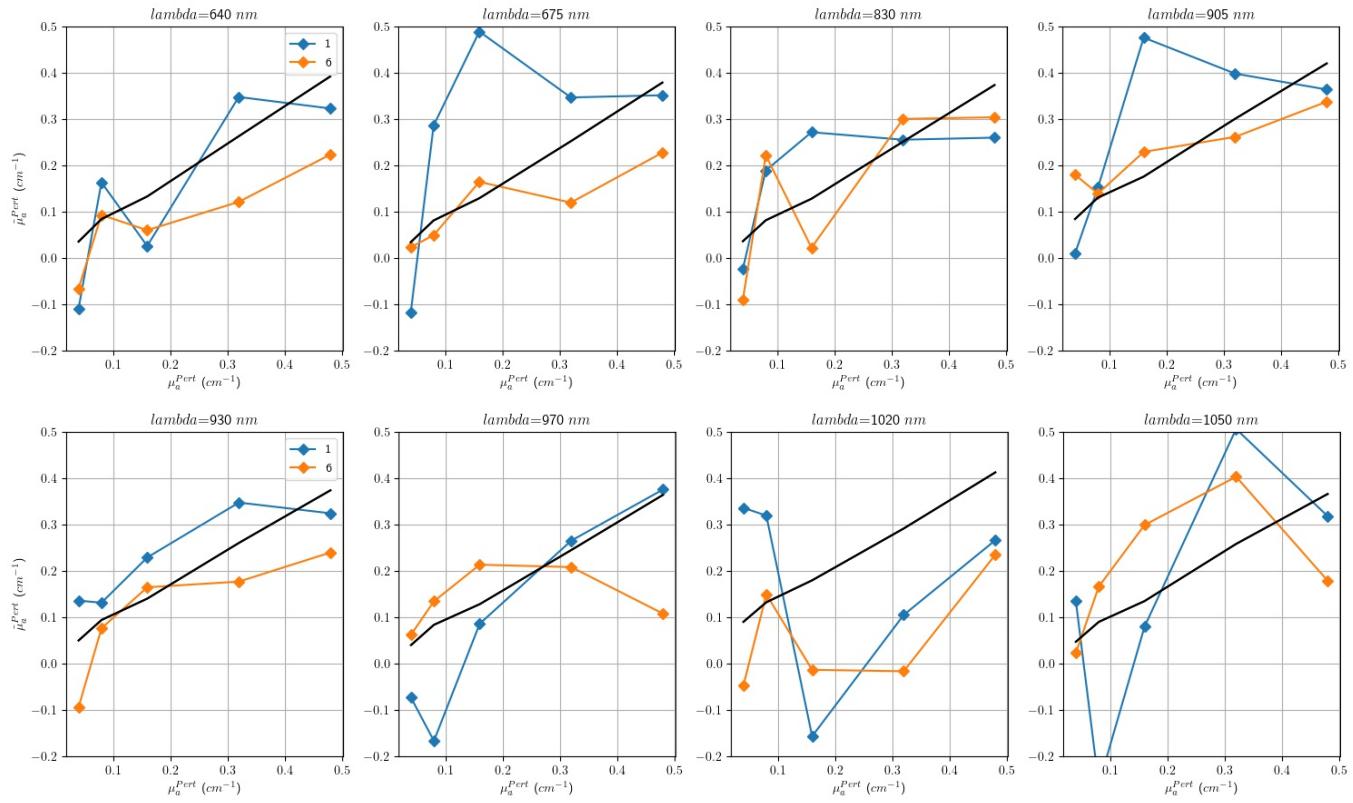

Figure 11. Linearity of the reconstructed absorption perturbation: measured absorption perturbation (y-axes) as a function of the nominal absorption perturbation (x-axes) for the two sizes of inhomogeneities (volume in the legend in cm^3). Different panels correspond to different wavelengths. The black line is the expected value. The regularization parameter is set to 0.01.

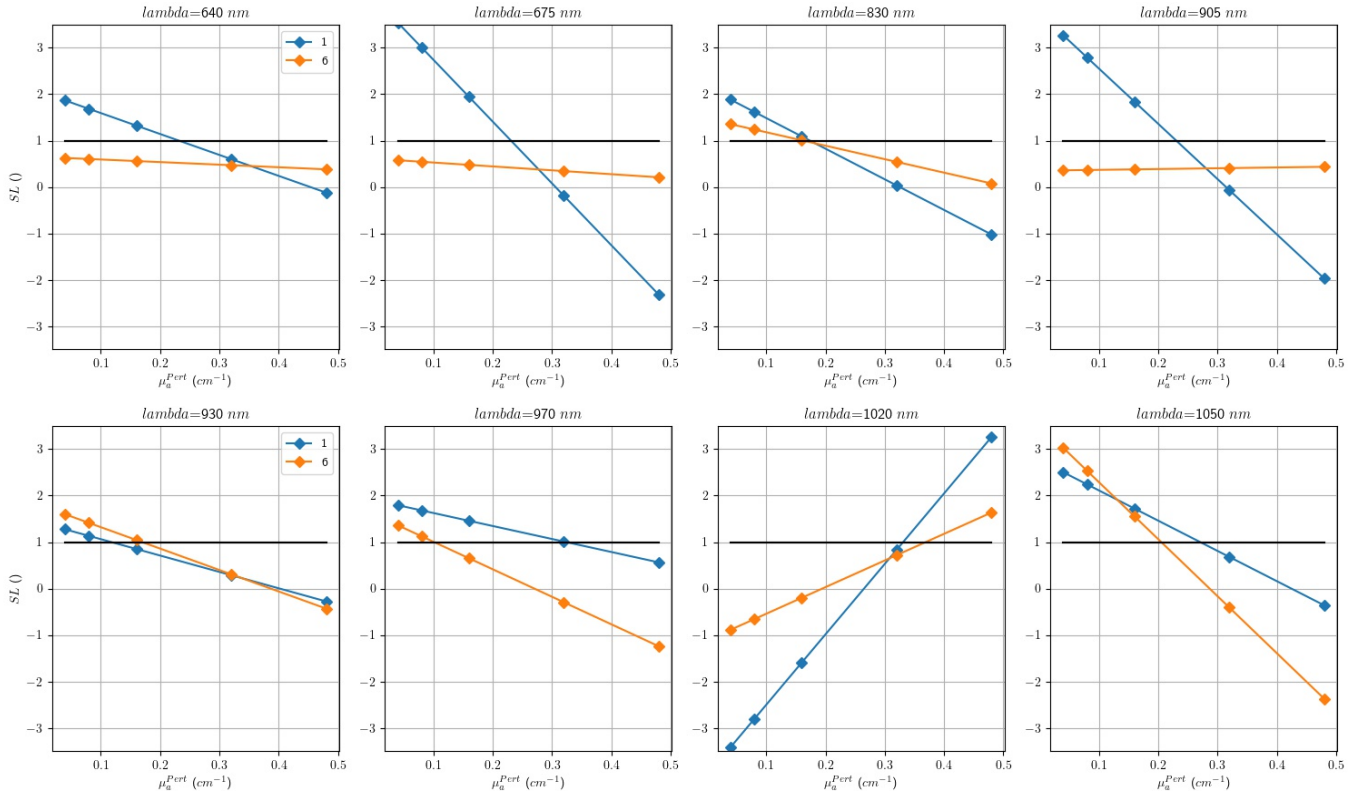

Figure 12. Slope of the absorption linearity plot (y-axes) as a function of the nominal absorption perturbation (x-axes) for the two sizes of inhomogeneities (volume in the legend in cm³). Different panels correspond to different wavelengths. The black line is the expected value. The regularization parameter is set to 0.01.

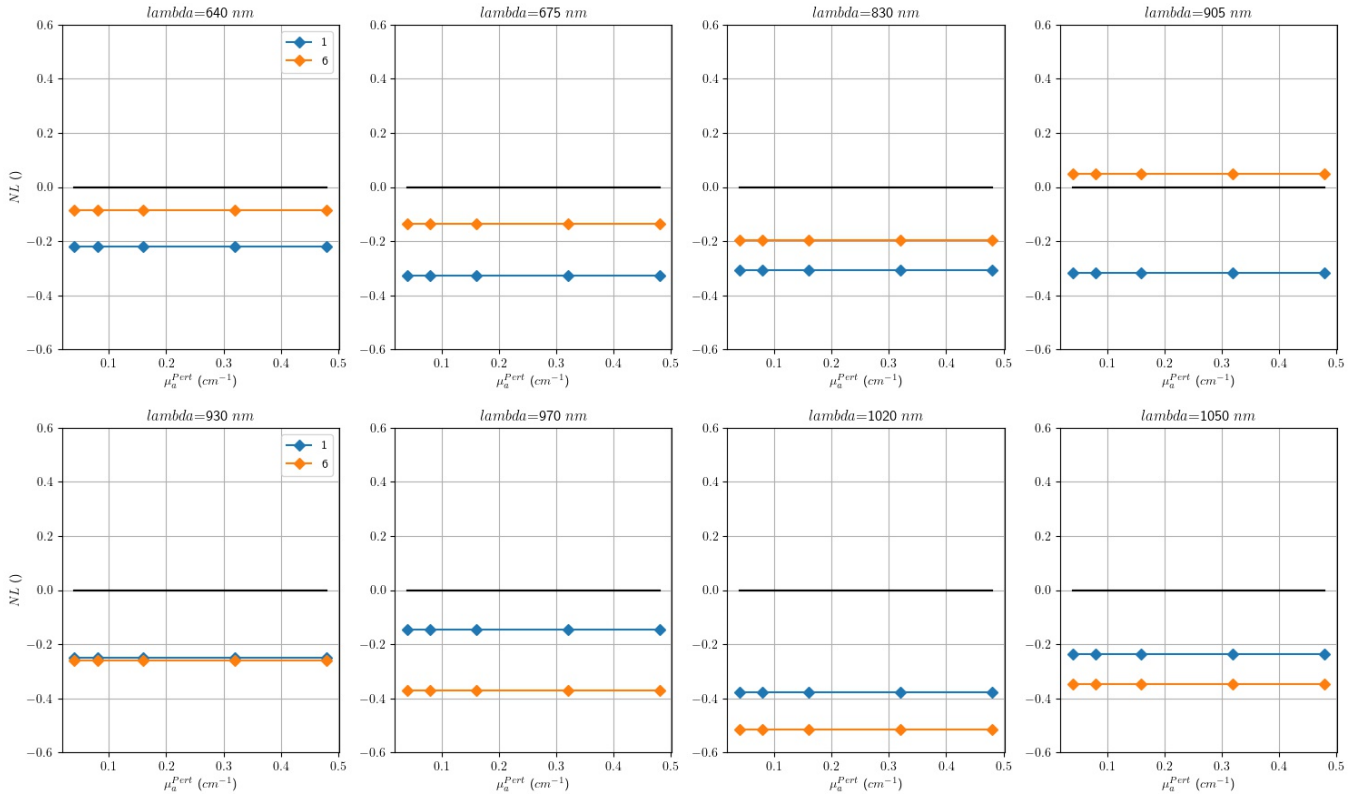

Figure 13. Absorption Non-Linearity (y-axes) as a function of the nominal absorption perturbation (x-axes) for the two sizes of inhomogeneities (volume in the legend in cm³). Different panels correspond to different wavelengths. The black line is the expected value. The regularization parameter is set to 0.01.

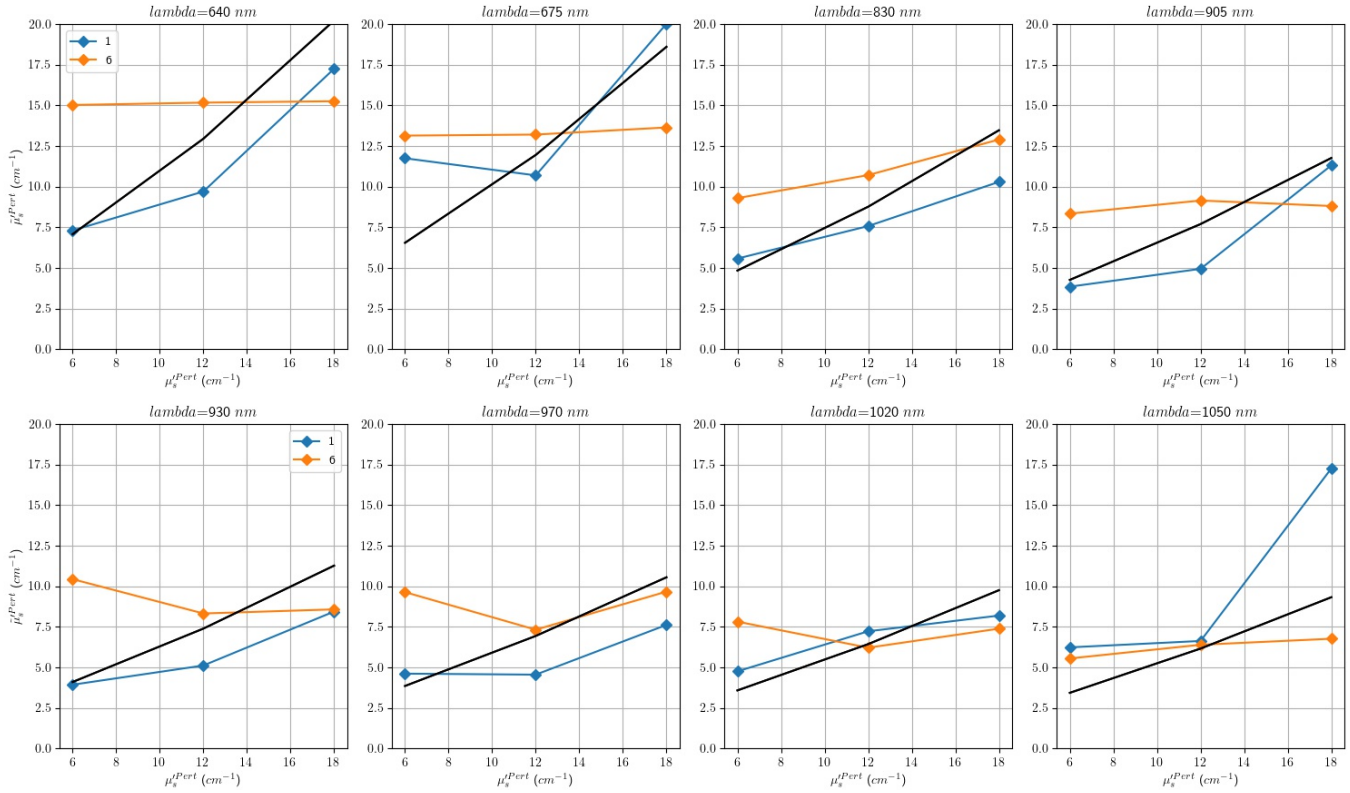

Figure 14. Linearity of the reconstructed scattering perturbation: measured scattering perturbation (y-axes) as a function of the nominal scattering perturbation (x-axes) for the two sizes of inhomogeneities (volume in the legend in cm³). Different panels correspond to different wavelengths. The black line is the expected value. The regularization parameter is set to 0.1.

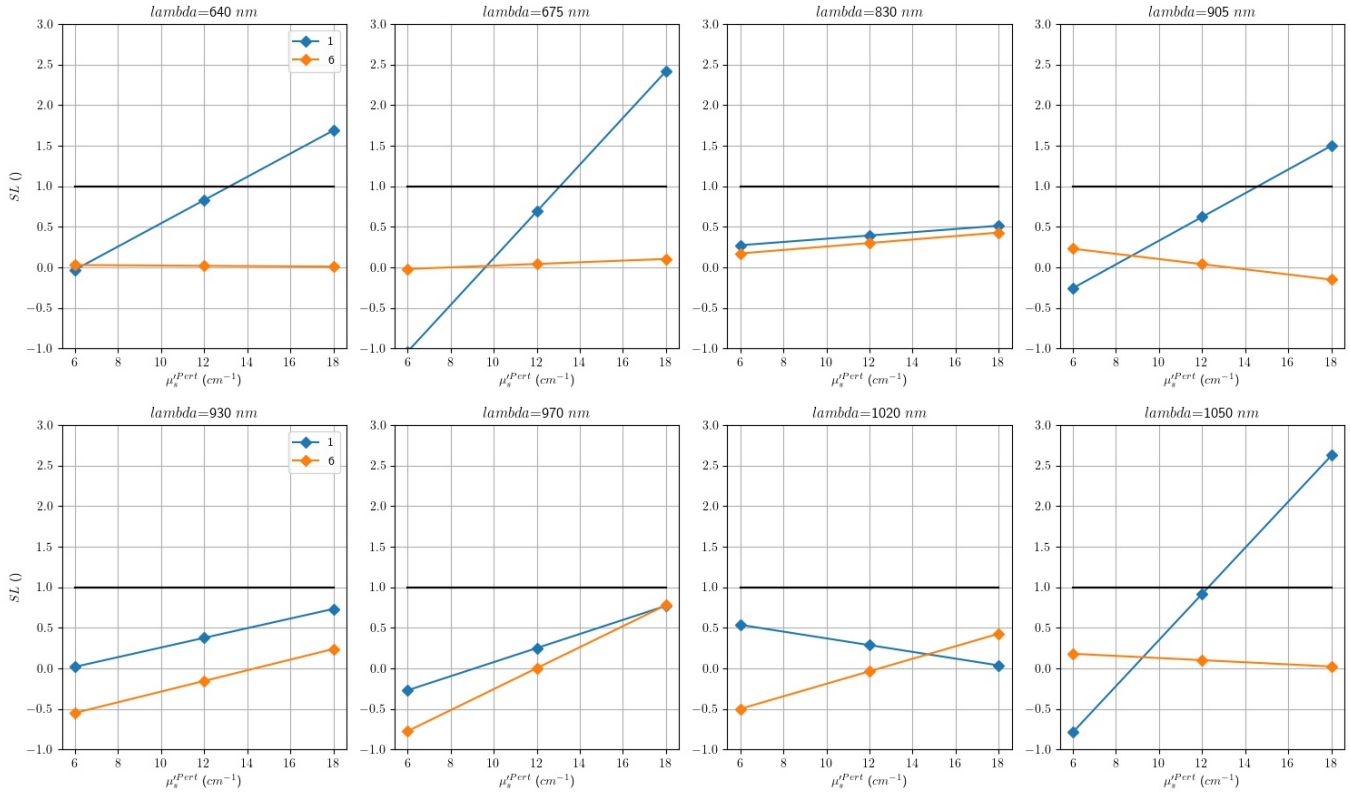

Figure 15. Slope of the scattering linearity plot (y-axes) as a function of the nominal scattering perturbation (x-axes) for the two sizes of inhomogeneities (volume in the legend in cm³). Different panels correspond to different wavelengths. The black line is the expected value. The regularization parameter is set to 0.1.

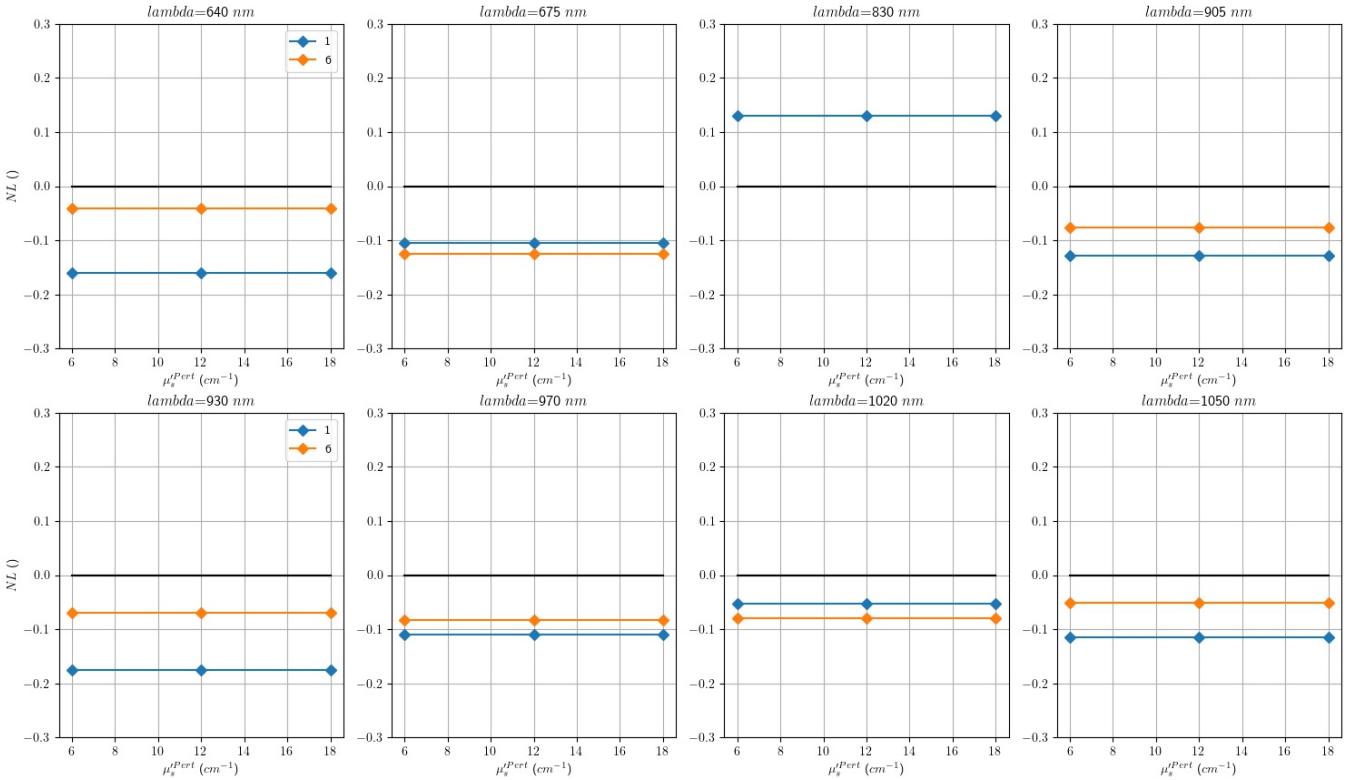

Figure 16. Scattering Non-Linearity (y-axes) as a function of the nominal scattering perturbation (x-axes) for the two sizes of inhomogeneities (volume in the legend in cm³). Different panels correspond to different wavelengths. The black line is the expected value. The regularization parameter is set to 0.1.

6. Conclusions

In conclusion, we have applied the SOLUS Protocol for the performance assessment of Diffuse Optics Tomographers – as defined in Deliverable D4.2 – on the SOLUS prototype. The test was performed using the specific inhomogeneous phantoms developed within SOLUS and described in Deliverable D4.4. The *Sensitivity* section of the protocol showed acceptable results for an absorption inhomogeneity with a *contrast* in the range of 100% for most of the wavelengths and a perturbation $\mu_a^{Pert} \geq 0.08$ cm^{-1}, while the *CNR* is hampered by the high noise in reconstruction. The *Localization* properties are very good with a displacement generally < 2 mm and a broadening < 4 mm even for the largest inclusions. This is a clear consequence of the use of the *a priori* information on the lesion geometry in the regularization algorithm. For what concerns *Quantitation* of the lesion properties, the *accuracy* is rather poor with an error <50% even for the two strongest perturbations, while the *linearity* is slightly more acceptable with the reconstructed perturbations following a positive correlation with the true values in almost all cases and a slope around 50÷200% (expected value 100%) and a non-linearity generally causing an underestimation by 20% for increasing absorption.

The key problem highlighted by the SOLUS Protocol is the large noise in reconstruction, causing large dispersion of recovered values. The reason could be the significant loss of information caused by the failure of 5 detectors out of 8, and of some firing wavelengths. A substantial improvement is expected from the second fully operational probe, which is being completed now and will be made fully available for the continuation of the SOLUS initial validation for up to 2 more years, as agreed in the SOLUS Consortium Agreement. Further, for the *in vivo* measurements, we are going to apply a spectrally-constrained reconstruction which proved effective for the analysis of *in vivo* time domain diffuse optical data collected at 7 wavelengths (635-1060nm) with an optical mammograph previously developed by POLIMI [5],[6]. In the spectrally-constrained approach only the concentrations of 5 tissue absorbers (oxy- and deoxyhaemoglobin, water, lipids, collagen) in addition to 2 scattering parameters (scattering amplitude

and slope) are used as unknown variables, instead of the 16 individual optical parameters. Besides the reduction in the number of variables (from 16 to 7) the spectrally-constrained analysis will create a constrain among tomographies at different wavelengths, possibly reducing the dispersion in reconstructed values. This method was not tested on the silicone phantoms, as they cannot reproduce the spectral shape of biological tissues, but was successfully tested on simulations (joint SOLUS paper in preparation by UCL and POLIMI). Both the spectrally unconstrained and the spectrally-constrained methods will be applied for the analysis of all SOLUS clinical data. This means also that the fulfilment of KPI5 – "*SOLUS prototype – Discrimination performances: number of independent parameters (e.g. Tissue constituents) which can be quantified in a suspect lesion by DOT*" which was initially linked to phantom data will instead be tested on *in vivo* data.

7. References

[1] G. Di Sciacca, L. Di Sieno, A. Farina, P. Lanka, E. Venturini, P. Panizza, A. Dalla Mora, A. Pifferi, P. Taroni, and S. R. Arridge, "Enhanced diffuse optical tomographic reconstruction using concurrent ultrasound information," Philos. Trans. R. Soc. A Math. Phys. Eng. Sci. 379, 20200195 (2021).

[2] L. Di Sieno; R. Cubeddu; H. Sportouche; D. Savéry; S. Konugolu Venkata Sekar; B. Rosinski; A. Farina; E. Ferocino; P. Lanka; P. Taroni; A. Pifferi; A. Dalla Mora "Solid heterogeneous phantoms for multimodal ultrasound and diffuse optical imaging: an outcome of the SOLUS project for standardization," in Novel Biophotonics Techniques and Applications V (2019), vol. 1107516.

[3] S. Konugolu Venkata Sekar, A. Dalla Mora, I. Bargigia, E. Martinenghi, C. Lindner, P. Farzam, M. Pagliazzi, T. Durduran, P. Taroni, A. Pifferi, and A. Farina, "Broadband (600-1350 nm) Time-Resolved Diffuse Optical Spectrometer for Clinical Use," IEEE J. Sel. Top. Quantum Electron. 22, 7100609 (2016).

[4] I. Pirovano, R. Re, A. Candeo, D. Contini, A. Torricelli, and L. Spinelli, "Instrument response function acquisition in reflectance geometry for time-resolved diffuse optical measurements," Biomed. Opt. Express 11, 240-250 (2020).

[5] G. Quarto, L. Spinelli, A. Pifferi, A. Torricelli, R. Cubeddu, F. Abbate, N. Balestreri, S. Menna, E. Cassano, and P. Taroni, "Estimate of tissue composition in malignant and benign breast lesions by time-domain optical mammography," Biomed. Opt. Express 5, 3684-3698 (2014).

[6] P. Taroni, G. Quarto, A. Pifferi, F. Abbate, N. Balestreri, S. Menna, E. Cassano, and R. Cubeddu, "Breast Tissue Composition and Its Dependence on Demographic Risk Factors for Breast Cancer: Non-Invasive Assessment by Time Domain Diffuse Optical Spectroscopy," PLoS ONE 10(6): e0128941 (2015).